Transport in Porous Media (2020) 135:713–734
https://doi.org/10.1007/s11242-020-01497-8

Pore-Scale Water Vapor Condensation Behaviors in Shales: An Experimental Study

Guijie Sang[1] · Shimin Liu[1] · Derek Elsworth[1] · Rui Zhang[1] · Markus Bleuel[2,3]

Received: 14 March 2020 / Accepted: 21 October 2020 / Published online: 3 November 2020

Abstract

Water condensation in shales impacts its hydro-mechanical response. A mechanistic understanding of the pore-water system is made more challenging by significant anisotropy of pore architecture and nano-scale heterogeneity of pore surfaces. We probe the condensation response in two contrasting shales exposed to a vapor of contrast-matching water, as characterized by in situ ultra-small/small-angle neutron scattering (USANS/SANS) techniques under various relative humidities. One shale with a higher content of both kerogen and clay has rougher surfaces and higher anisotropy than the other shale (less clay and no kerogen) over length scales from 2.5 to 250 nm. Scanning electron microscopy with energy-dispersive spectrometry (SEM–EDS) analysis also confirms that the organic-rich shale presents more anisotropic microfabrics and higher heterogeneity compared to the other shale with less clay and no kerogen. USANS/SANS results show that water condensation effectively narrows the pore volume in the way of reducing the aspect ratio of non-equiaxed pores. For the shale with less clays and no kerogen under a relative humidity of 83%, a wetting film uniformly covers the pore-matrix interface over a wide range of length scale (1 nm–1.9 μm) without smoothing the surface roughness. In contrast, for the organic-rich and clay-rich shale with a strong wetting heterogeneity, condensation occurs at strongly curved hydrophilic asperities (1–10 nm) and smoothens the surface roughness. This is consistent with water vapor condensation behavior in a Vosges sandstone by Broseta et al. (Phys. Rev. Lett. 86:5313, 2001). Though well representing the condensation behavior of water vapor in mesopores/macropores (radii > 1 nm), USANS/SANS techniques could underestimate total water adsorption due to potential cation hydration and clay swelling in micropores (radii < 1 nm).

Keywords Capillary condensation · Neutron scattering · Pore anisotropy · Surface roughness

Electronic supplementary material The online version of this article (https://doi.org/10.1007/s11242-020-01497-8) contains supplementary material, which is available to authorized users.

✉ Shimin Liu
szl3@psu.edu

Extended author information available on the last page of the article

1 Introduction

Shale is a fine-grained and porous sedimentary rock comprising an aggregate of various clay and other minerals/kerogen. Water penetration can alter the pore-scale properties of the shale, including changes in gas storage due to alteration of the pore structure, changes in gas permeability as a result of pore occlusion by liquid water, mechanical degradation due to the reduction of surface energy and/or mineral swelling, and the formation of hydrate in shales or sediments serving as hydrocarbon sources and/or sealing reservoirs. An improved understanding of the water condensation behavior at pore-scale is a basic prerequisite in deconvolving the role of water on hydrocarbon extraction (Eveline et al. 2017), CO_2 trapping (Andrew et al. 2014), wellbore stability (Ghassemi and Diek 2002), injection induced-seismicity (Elsworth et al. 2016), roof control in underground coal mining (Van Eeckhout 1976), and the formation of gas hydrates (Hesselbo et al. 2000), among others.

Shale-water interactions at pore scale are known to be complex. This complexity stems from the hydrogen-bonded nature of water (Luzar and Chandler 1996) and the interplay of serval factors including mineral type (Sposito et al. 1999), heterogeneity of kerogen and their spatial distribution (Bousige et al. 2016; Chiang et al. 2018; Yang et al. 2017), pore size distribution (Clarkson et al. 2013; Kuila and Prasad 2013; Sang et al. 2018; Zhao et al. 2019), and pore connectivity (Liu et al. 2019; Melnichenko et al. 2012; Ruppert et al. 2013; Zhang et al. 2015). Firstly, variations in the distribution of minerals/kerogen with different wetting characteristics further impart strong wetting heterogeneity (Van Lingen et al. 1996). This strong wetting heterogeneity, also associated with the pore surface roughness (AlRatrout et al. 2018), makes it difficult to characterize levels and distributions of capillary condensation based on Kelvin theory and/or other models (BJH; Barrett et al. 1951; Fisher et al. 1981), even if the pore-scale architecture may be otherwise imaged. Secondly, shales have a preferred orientation of particles/minerals as well as intervening pore structure sub-parallel to bedding as a result of long-term sedimentary compaction (Lash and Blood 2004; Loon 2008). This structural anisotropy imparts anisotropy in hydro-mechanical properties of diffusivity (Van Loon et al. 2004), permeability (Blunt and King 1991; Hannon and Finsterle 2018), strength and modulus, and related acoustic velocities (Chichinina et al. 2009). Quantifying water vapor condensation behavior in such preferentially oriented pores is crucial to recognize the role of water in these hydro-mechanical properties under a partial pressure of water vapor. Unfortunately, due to the multi-component character of shale with strong heterogeneity and pore anisotropy, it is very challenging to characterize the pore-scale water vapor condensation behavior based on traditional physisorption measurement and imaging techniques.

Although mechanisms and impacts of water vapor adsorption in shales have been extensively reported, typically based on traditional gravimetric methods (Sang et al. 2020, 2019; Seemann et al. 2017; Zolfaghari et al. 2017), limited studies probe the pore-scale condensation mechanisms and rationalize observed response. This is principally due to the innate complexity of the heterogeneity and anisotropy together with challenges related to the multi-scale pore structure as just mentioned. The distribution of water sorption in pore networks has been effectively probed by N_2/CO_2 physisorption in moisture equilibrated mudstone/shale samples (Lahn et al. 2020; Zou et al. 2020). However, N_2/CO_2 physisorption may be influenced by the effect of capillary occlusion by condensed water at pore throats. Besides, N_2 physisorption measurement at 77 K on the moisture equilibrated mudstone/shale samples may also be subjected to the effect of water expansion due to freezing. Consequently, the effects of capillary occlusion and/or water expansion on the N_2/CO_2

physisorption measurement will in turn influence the interpretation of the distribution of liquid water in the pore network. Furthermore, it remains challenging to understand the effect of water condensation in altering structural anisotropy and surface roughness, based solely on conventional physisorption methods. An in situ small-angle neutron scattering (SANS) technique may be an alternative to solve these challenges.

Compared to traditional physisorption methods, SANS is a noninvasive method for characterizing rock structure and pore-scale rock-fluid interaction (Bahadur et al. 2014; Hall et al. 1998; Liu and Zhang 2020). SANS intensity $I(Q)$, or neutron cross section per unit volume (in cm^{-1}), for a two-phase (matrix and pore) rock with randomly distributed pores can be expressed as follows:

$$I(Q) = 4\pi\left(\rho_s^* - \rho_f^*\right)^2 \phi(1-\phi) \int_0^\infty r^2 \gamma_0(r) \frac{\sin Qr}{Qr} \mathrm{d}r \tag{1}$$

where $\left(\rho_s^* - \rho_f^*\right)^2$ is the neutron contrast between the scattering length density (SLD) of rock solids (ρ_s^*) and SLD of fluid in pores (ρ_s^*); ϕ is the total porosity of the rock sample illuminated by the neutron beam; the scattering vector $Q = 4\pi\lambda^{-1}\sin(\theta/2)$ and λ and θ are the neutron wavelength and the scattering angle, respectively; $\int_0^\infty r^2\gamma_0(r)\frac{\sin Qr}{Qr}\mathrm{d}r$ is the Fourier transform of the correlation function $\gamma_0(r)$. From the above equation, the measured SANS intensity $I(Q)$ in a rock system is attributed to the neutron contrast $\left(\rho_s^* - \rho_f^*\right)^2$ between SLDs of the rock solids and pore fluids. Provided that voids/pores are intruded/occupied by a fluid with its SLD equals the rock solid, these occupied (or contrast-matched) voids/pores would no longer contribute to the total scattering intensity. In this way, one may quantify the intruded fluids based on relevant models as detailed in the future sections.

We apply in situ ultra-small-angle and small-angle neutron scattering (USANS/SANS) techniques to characterize water (contrast-matching mixture of D_2O/H_2O) condensation behavior in the anisotropic pore architecture of two shales under a spectrum of relative humidities (RH: 0–88%). At a specific partial pressure of the D_2O/H_2O vapor, the pore spaces occupied by the condensed contrast-matching D_2O/H_2O mixture no longer contribute to the neutron scattering intensity and thus may be quantified by the USANS/SANS technique in terms of the evolution of the degree of anisotropy, surface roughness, and pore size distribution at various relative humidities. These results are anchored against traditional macroscale measurements involving dynamic vapor sorption methods (DVS) to correlate responses across spatial scales.

2 Materials and Methods

2.1 Mineralogical Compositions

The two shale samples were collected from the roof strata of two coal seams in Illinois Basin, one from Hymera (VI) coal seam at Bear Run Mine, Carlisle, Indiana, USA, the other from Herrin (No. 6) coal seam at Wildcat Hills Mine Equality, Illinois, USA. They are labeled as "*Hymera*" and "*Herrin*," respectively. Chemical compositions were analyzed by X-ray diffraction (XRD) for mineral composition and by ultimate analysis for kerogen (Sang et al. 2018). Ultimate analysis of carbon, hydrogen, and nitrogen, following the standard test method—ASTM D5373, presents 24.7% carbon, 2.5% hydrogen, and 0.41%

nitrogen (by weight), respectively. Total organic carbon (TOC) content was obtained by subtracting inorganic carbon quantified from XRD analysis from total carbon as quantified by ultimate analysis. We also conducted the vitrinite (R_0) analysis and quantified the functionalized oxygen-to-carbon (O/C) atomic ratio in kerogen for the *Herrin* shale. As shown in Table 1, *Hymera* shale comprises 14.2% quartz and 85.8% phyllosilicate minerals including 21.5% illite, 29.3% muscovite, 28.9% clinochlore, 3.4% dickite, and 2.7% albite. *Herrin* shale comprises 17.7% quartz, 54.5% phyllosilicates, including 8.6% montmorillonite, 29.3% illite, 5% muscovite, and 11.6 halloysite. *Herrin* shale also contains minor fractions of pyrite (3.1%) and dolomite (3.3%). In addition, *Herrin* shale contains 21.4% TOC with the vitrinite reflectance (R_0) of 0.71% and the oxygen-to-carbon (O/C) atomic ratio of 5.0%. The carbon-to-hydrogen atomic ratio (H/C) based on the ultimate analysis is 1.22. Therefore, kerogen in *Herrin* shale belongs to Type II. The distribution of kerogen, as shown based on the scanning electron microscopy (SEM) images in Sect. 2.2, and its overall hydrophobicity of kerogen leads to strong wetting heterogeneity of *Herrin* shale. Scattering length densities (SLDs) are calculated as 3.6×10^{-10} cm^{-2} for the *Hymera* shale and 3.8×10^{-10} cm^{-2} for the *Herrin* shale, using a weighted average of volume over all chemical components (Bahadur et al. 2014; Radlinski et al. 1996). The calculated SLD values based on the chemical components provide a reference for adjusting the ratio of deuterium oxide and hydrogen oxide (D_2O/H_2O) to achieve the contrast matching condition when condensation occurs.

2.2 Scanning Electron Microscopy (SEM)

The fabric of the two shales and their elemental compositions were identified by SEM with energy-dispersive spectrometry (SEM–EDS). SEM images of the two shales are shown in Fig. 1a–h. *Hymera* shale, barren of organic matters (Fig. 1a–d, presents a relatively random particle microfabric lack of lamination. The lack of anisotropy of the *Hymera* shale could be due to shale bioturbation, which tends to randomize clay particle fabric and decrease the fissility of shale (Byers 1982, 1974; O'Brien 1987). In contrast, the organic-rich *Herrin* shale (Fig. 1e–h) presents a high degree of preferred orientation of particles as well as pores. This is also consistent with previous SEM studies (O'Brien 1987) on organic-rich black shales, which showed preferentially oriented microfabrics due to the lack of bioturbation. Note that these SEM images are in the micron scale, which may not well capture mesopores (< 50 nm) and macropores smaller than 250 nm. The preferential orientation

Table 1 Weight percentage of the mineralogical compositions[a] for the two shale samples (%)

Sample	Phyllosilicate minerals										
	Quartz	Illite	Musc.	Clin.	Dickite	Albite	Mont.	Hall.	Pyrite	Dolo.	TOC[b]
Hymera	14.2	21.5	29.3	28.9	3.4	2.7	–	–	–	–	–
Herrin	17.7	29.3	5.0	–	–	–	8.6	11.6	3.1	3.3	21.4

[a]*Musc.* denotes muscovite; *Clin.* denotes clinochlore; *Mont.* denotes montmorillonite; *Hall.* denotes halloysite; *Dolo.* denotes dolomite. *TOC* refers to total organic carbon

[b]*TOC* content (21.4%) was obtained by subtracting inorganic carbon in dolomite from total carbon as quantified by ultimate analysis. The vitrinite reflectance (R_o) of kerogen was measured as 0.71%. The functionalized oxygen-to-carbon (O/C) atomic ratio is 5.0% (±1.6%), which was estimated by X-ray photoelectron spectroscopy

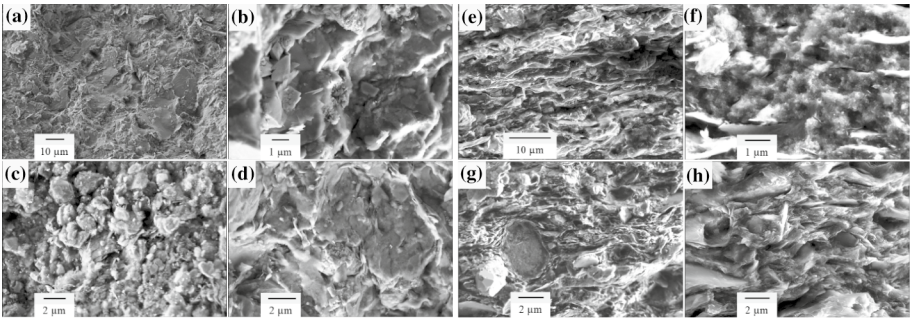

Fig. 1 SEM images showing variations of the microfabric for (**a–d**) *Hymera* shale and (**e–h**) *Herrin* shale

of these nanopores will be quantified based on the SANS study on thin sections of the two shales, as detailed in Sect. 3.1.

The elemental compositions of the two shales were also identpercentage of the mineralogical compositions ified by SEM–EDS spectrum analysis as shown in Figs. 2 and 3, respectively. *Hymera* shale (Fig. 2) mainly consists of the following elements: O, Al, Si, Fe, S, K, Mg, and Na, while lacks of carbon. At different locations of the SEM image as shown in Fig. 2a, the EDS spectrums present the same types of elemental compositions and hence indicate that *Hymera* shale is relatively homogenous in terms of its mineral

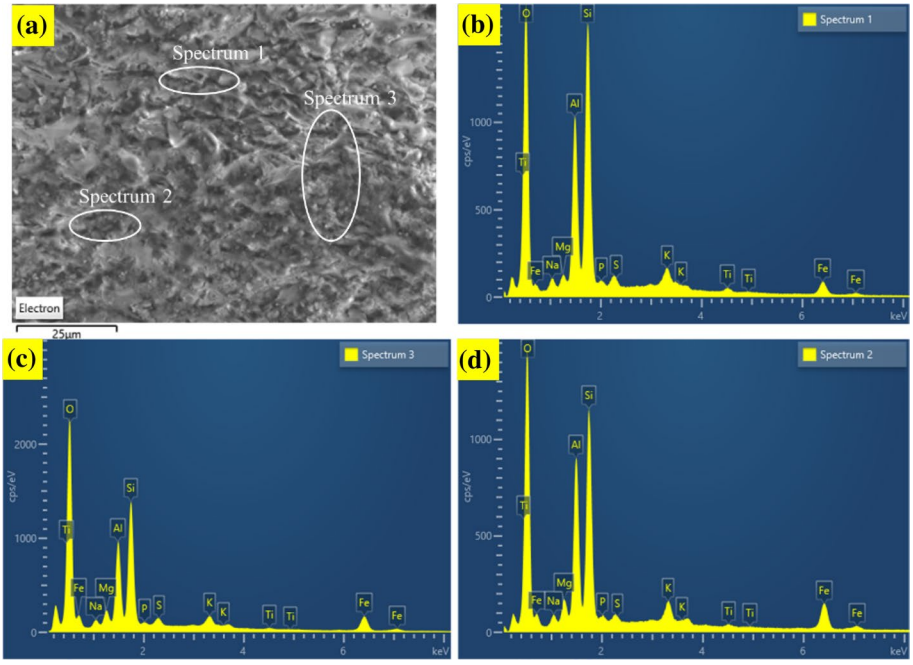

Fig. 2 SEM–EDS analysis of the *Hymera* shale. **a** SEM image; **b–d** EDS spectrums of the three selected elliptical zones as marked in the SEM image. The three spectrums show similar elemental compositions and indicate that the *Hymera* shale is relatively homogeneous

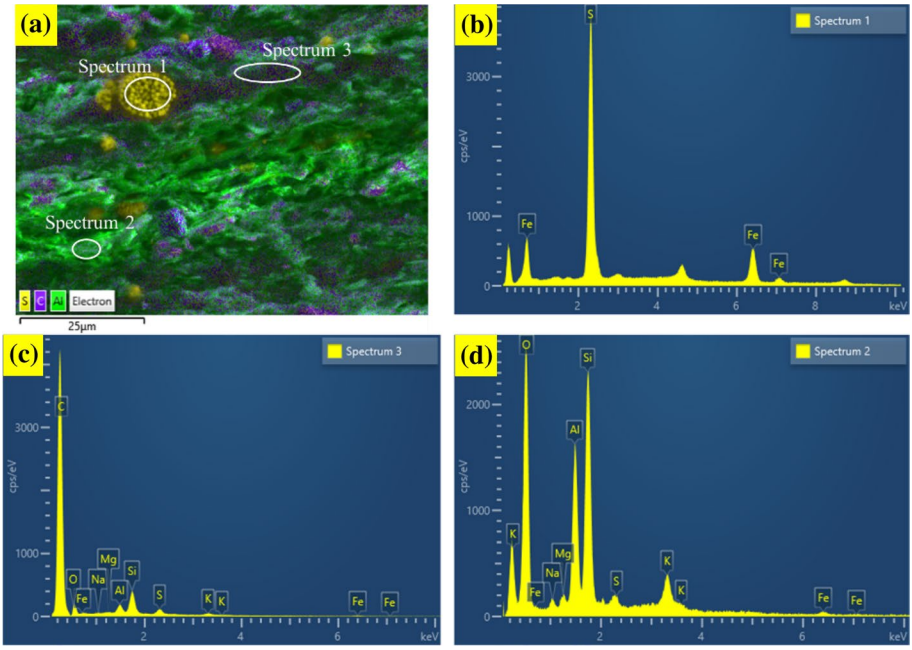

Fig. 3 SEM–EDS analysis of the *Herrin* shale. **a** EDS layered image displaying the distributions of sulfur, carbon, aluminum, and SEM image; **b** EDS spectrum of pyrite (FeS_2); **c** EDS spectrum indicating a high content of organic matters; **d** EDS spectrum indicating a high content of aluminum phyllosilicate (or clay). The layered image shows a strong heterogeneous distribution of different minerals and scattered organic matters

types. The lack of organic matters in *Hymera* shale also leads to a more homogeneous wettability, which belongs to hydrophilicity due to the presence of inorganic minerals. In contrast, the EDS spectrums of the organic-rich *Herrin* shale, as shown in Fig. 3, show great discrepancy at three different locations and indicate a strong heterogeneous distribution of different minerals and organic matters. One can also observe from Fig. 3a that *Herrin* shale presents scattered organic matters embedded in inorganic minerals, which could cause a strong wetting heterogeneity considering the hydrophobicity of organic matters and the hydrophilicity of the inorganic minerals. The mineral/kerogen types of the two shales identified by SEM–EDS analysis are overall consistent with the mineralogical compositions as shown in Sect. 2.1.

2.3 In Situ SANS Experiment

For the USANS/SANS experiments, the environment was humidity-controlled by using a 60% D_2O to 40% H_2O mixture (by weight) with an SLD in the liquidus of approximately 3.6×10^{-10} cm^{-2}. The purpose of applying this mixture is to minimize the scattering contrast between the shale matrix and condensed water. Although the two-phase assumption may not give an accurate SLD of the solid matrix, due to the chemical heterogeneity of shale, this approach has been widely accepted and adopted since the contribution of chemical inhomogeneity to total scattering is usually less than 5–10% (Hall et al. 1998; Melnichenko et al. 2012; Radlinski et al. 2004). Based on the two-phase

scattering assumption, pores occupied by the contrast-matching condensed D_2O/H_2O will not contribute to neutron scattering–rendering the pores neutron transparent. Thus, the degree of water condensation in the pores can be directly quantified by comparison between the scattering patterns recovered under dry then prescribed humidity conditions. Furthermore, since water sorption in the two shales presents no permanent hysteresis in water content to RH over three cycles (see supporting information Figure S1), the water sorption involves the only physisorption with no irreversible alteration of pore structure during the ad-/de-sorption process. Absent chemical interactions, we assume that the isotopic exchange of hydrogen between particle surfaces and the D_2O/H_2O mixture under the in situ water vapor conditions is negligible at a laboratory time scale (Ruppert et al. 2013).

SANS experiments on thin prismatic sections (150 μm) of the two shales (Fig. 4) were performed in this controlled in situ water vapor environment using the CHRNS 30 m SANS instrument at the Center for Neutron Research (NCNR) of the US National Institute of Standards and Technology (US-NIST). The sample-to-detector distances were chosen as 1 m, 4 m, 13 m, and 13 m with a lens to cover a total range of the scattering vector of $0.0015\ \text{Å}^{-1} < Q < 0.3\ \text{Å}^{-1}$. The neutron wavelength λ was set at 6 Å with a wavelength spread $\Delta\lambda/\lambda$ of 0.138. USANS experiments were performed using the high-resolution BT5 perfect crystal diffractometer ($\lambda = 2.4$ Å, $\Delta\lambda/\lambda = 6\%$) at NCNR, with Q ranging from 3×10^{-5} to $0.0011\ \text{Å}^{-1}$. The pore size was estimated from an empirical relationship between pore radius r of a polydisperse porous medium and the scattering vector Q as (Radliński et al. 2000): $r \approx 2.5/Q$. Relative humidity during the in situ USANS/SANS measurement was controlled by two mass flow controllers (MFCs) by adjusting the ratio of dry gas to saturated water vapor, which was generated by a bubbler inserted into the liquid D_2O/H_2O mixture. The temperature in the humidity cell was maintained at ~23 °C to avoid any potential for the condensation of water droplets on the shale surfaces. For each humidity condition, the dew point (< 23°) was also monitored throughout the whole USANS/SANS procedure.

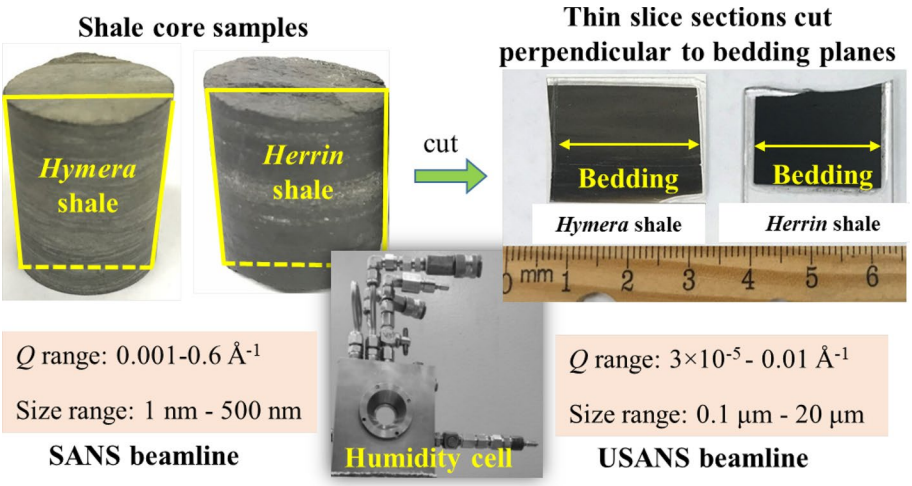

Fig. 4 SANS/USANS measurements on shale thin sections at different relative humidities. The samples were cut perpendicular to their bedding planes with to a thickness of 150 μm and mounted on a quartz slice for mechanical support

The two shales were cut perpendicular to bedding planes into thin prismatic sections (Fig. 4). This particular orientation is to probe the structural anisotropy of the shales using a single normally incident neutron beam, as shown in Fig. 5a. Figure 5b shows a typical example of a two-dimensional (2D) SANS spectrum with elliptical scattering contours resulting from the structural anisotropy. The 1D scattering cross section $I(Q)$ is shown relative to each of azimuthal angle φ and scattering vector Q in Fig. 5c, d respectively—recovered from the 2D SANS spectrum. The non-uniform distribution of scattering intensities with respect to azimuthal angle (Fig. 5c) directly infers anisotropy in the structure of the shale. From Fig. 5c, d, the scattering intensity at the same length scale (Q value) shows a clearly higher magnitude at 90°, relative to 0°, in the reciprocal space. This corresponds to flattened pores preferentially aligned sub-parallel to bedding in real space (Hall et al. 1986). These observations enable pore anisotropy of the two shales to be characterized based on an alignment factor calculated from the 1D scattering cross section $I(Q)$ measured relative to azimuthal angle.

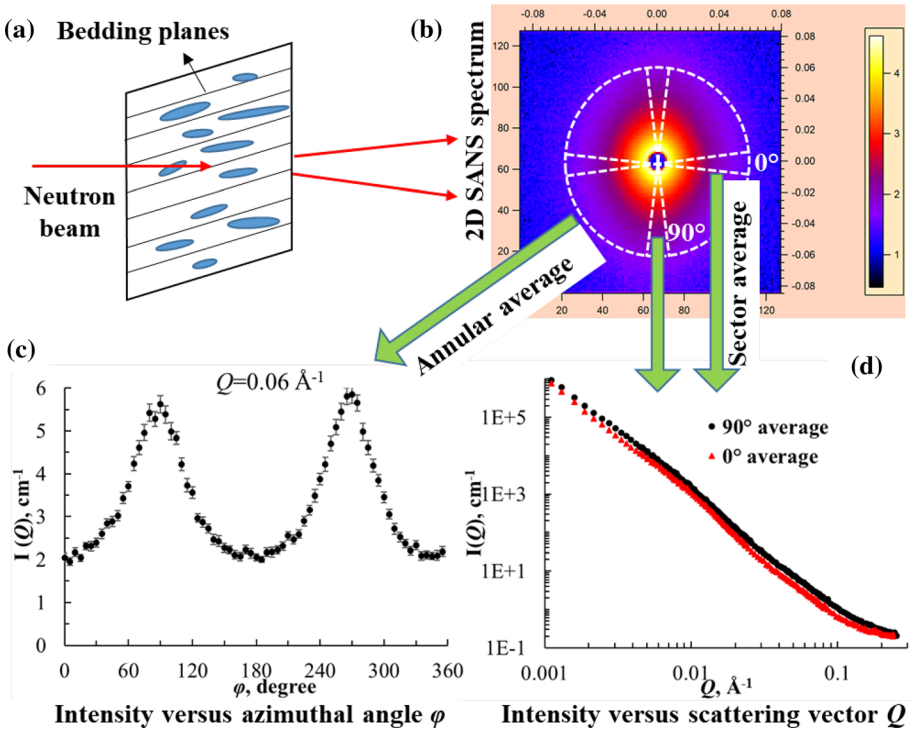

Fig. 5 Schematic representation of anisotropic pore structure of a shale imaged by SANS. **a** Thin sections cut perpendicular to bedding subjected to normal incidence; **b** 2D SANS spectrum illustrating elliptical scattering contours that suggests favorably aligned minerals/grains and pore structure; **c** one-dimensional scattering cross section $I(Q)$ versus azimuthal angle φ; and **d** $I(Q)$ versus scattering vector Q, reduced from the 2D SANS spectrum. Error bars for $I(Q)$ vs. Q are too small to be apparent

3 SANS Results and Discussion

3.1 Structural Anisotropy and Fractal Characteristics

Multi-scale structural anisotropy, from several Angstroms to several microns, is a pervasive feature in many shales but limited work has focused on quantifying the pore anisotropy (Anovitz et al. 2015; Gu et al. 2015; Hall et al. 1986; Leu et al. 2016; Liu and Zhang 2020). Figure 6 shows the combined SANS and USANS profiles under dry condition with the scattering intensity $I(Q)$ reduced in the directions parallel and perpendicular to bedding. SANS profiles were reduced from the 2-D scattering intensity distribution (Fig. 5b) by sector averaging at 0° and 90°, representing the structure both perpendicular and parallel to bedding, respectively. Slit-smeared USANS data, measured both perpendicular and parallel to bedding, were converted into the SANS pinhole geometry and then merged with the SANS data. Notably, for the same scattering vector, scattering intensity averaged at 90° (bedding-parallel) is larger than that at 0° (bedding-perpendicular). This implies the bedding-parallel extension, or bedding-perpendicular flattening, of pores as illustrated in Fig. 5a with a preferred orientation and resulting anisotropy. The *Herrin* shale appears more preferentially oriented or anisotropic than the *Hymera* shale—indexing by a larger discrepancy in the scattering intensities between the two directions (Fig. 6). This is consistent with the SEM images shown in Fig. 1 that *Herrin* shale presents a more preferentially oriented microfabric than *Hymera* shale. The *Herrin* shale exhibits the least discrepancy at a Q value of approximately 0.01 $Å^{-1}$, indicating the least anisotropy of pores with radii of the order of ~25 nm. The degree of pore anisotropy may be quantified based on an alignment factor.

Annularly averaging the scattering intensity distribution over the detector enables the scattering intensity $I(Q, \varphi)$ to be defined for the two shales as a function of azimuthal angle at different Q values (0.02 $Å^{-1}$, 0.04 $Å^{-1}$, 0.06 $Å^{-1}$, 0.08 $Å^{-1}$, 0.1 $Å^{-1}$) as shown in Figure S2 (Supporting information). Instead of being uniformly distributed over the range of azimuthal angles, from 0° to 360°, which is typically the case for a sample cut parallel to bedding and indicating a random orientation of pores (Gu et al. 2015), the scattering

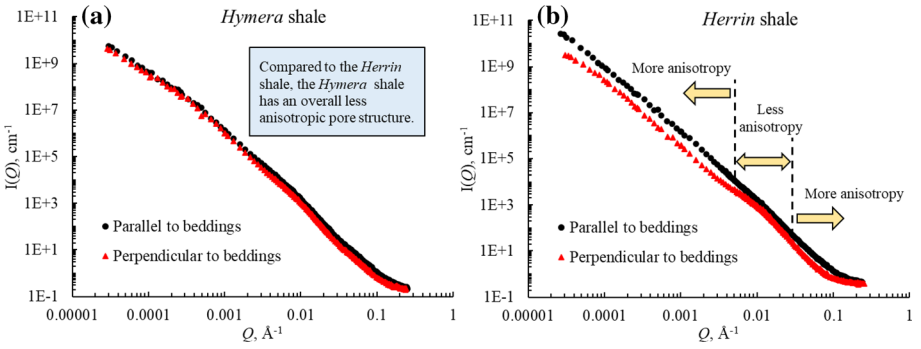

Fig. 6 Combined SANS and USANS scattering cross section $I(Q)$ versus scattering vector Q for both (**a**) the *Hymera* and (**b**) the *Herrin* shales under the dry condition. 1-D SANS data, both perpendicular and parallel to bedding, were reduced from 2-D scattering intensity distributions by sector averaging at 0° (minor axis) and 90° (major axis) with an incremental azimuthal angle of ± 10°. 1-D slit-smeared USANS data, measured in directions both perpendicular and parallel to bedding, were converted into the SANS pinhole geometry and then merged to the SANS data

intensities for these two shales (cut perpendicular to the bedding) show an approximately sinusoidal distribution with azimuth. The degree of preferential orientation of the pores can be quantified by an alignment factor $A_f(Q)$ given by the following equation (Hongladarom et al. 1996).

$$A_f(Q) = \frac{\int_0^{90^\circ} I(Q,\varphi)\cos 2\varphi \mathrm{d}\varphi}{\int_0^{90^\circ} I(Q,\varphi) d\varphi} \tag{2}$$

where the absolute value of $A_f(Q)$ approaches 1 for the case when scattering is concentrated solely at an azimuthal angle of 90°, representing the extremely preferential orientation of the non-equiaxed pores, or approaching 0 for an isotropic scattering distribution, representing randomly oriented pores. According to Eq. (2), the alignment factor over different Q ranges (0.002–0.1 Å^{-1}) for both the *Hymera* and *Herrin* shales were computed and are shown in Fig. 7. For Q in the range 0.002–0.1 Å^{-1}, corresponding to pore radii of 2.5–125 nm, the *Herrin* shale has overall larger alignment factors (0.13–0.34) than the *Hymera* shale (0.03–0.12), indicating more preferentially oriented pores and greater resulting anisotropy in the *Herrin* shale, which is consistent with the SEM results in Sect. 2.2. The degree of anisotropy also varies with the pore size as demonstrated in Fig. 7. Anisotropy decreases in the *Hymera* shale with increasing pore radii in the range 2.5–125 nm. Anisotropy in the *Herrin* shale decreases with increasing pore radius for mesopores (pore radii <25 nm) but increases with increasing pore radius for macropores (pore radii > 25 nm). These trends are also consistent with the 1-D scattering pattern plotted as a function of scattering vector Q in directions of both perpendicular and parallel to bedding, as shown in Fig. 6. Note that the alignment factors for Q in the range 0.002–0.1 Å^{-1} were obtained by reducing the 2D SANS spectrum. Pore anisotropy in the USANS region ($Q < 0.002$ Å^{-1}) were not quantified by these alignment factors—due to the fact that the 1-D slit-smeared USANS data were collected merely in the directions perpendicular and parallel to bedding (scattering intensity data are unavailable for intervening

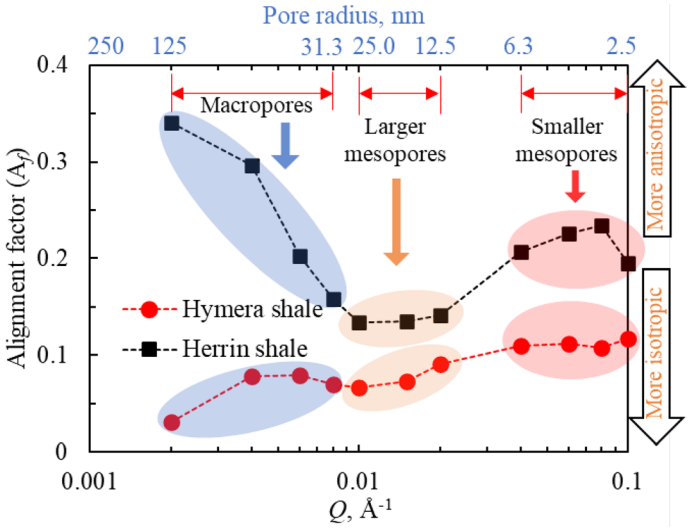

Fig. 7 Alignment factor A_f versus the scattering vector Q (proxy for pore radius) under dry conditions

azimuthal angles). From Fig. 6, at $Q < 0.002$ Å^{-1}, corresponding to macropore radii larger than 125 nm, the *Herrin* shale exhibits relatively high pore anisotropy while the *Hymera* shale exhibits relatively low pore anisotropy. Again, this is consistent with the SEM results (Fig. 1) regarding particle/pore orientation of the two shales.

Over length scales from a few nanometers to a few microns, the roughness of the pore-matrix interfaces can be quantitatively described by a fractal dimension f_D, estimated by the power-law exponent α and recovered from the slope of the SANS scatting pattern as (Bale and Schmidt 1984): $f_D = 6 - \alpha$. f_D approaches 2 for smooth interfaces and asymptotes to 3 for infinitely rough, volume filling, interfaces (Radliński et al. 1999; Wong et al. 1986; Zhang et al. 2017). From Fig. 6, the combined USANS and SANS profiles for the two shales, and especially for the *Herrin* shale, present a "hump" in the direction perpendicular to bedding for a Q approximately equal to 0.01 Å^{-1}—corresponding to a pore radius of 25 nm. This feature possibly results from the spatial ordering of flattened pores with a size ~25 nm and resulting from sedimentary compaction (Hall et al. 1986). Fractal dimensions for the two shales were estimated from the scattering pattern in the direction parallel to bedding (sector averaging at 90°), present as a straight line in log–log space (Supporting information Figure S3) and reflecting the power-law characteristics of fractal pore surfaces. As shown in Figure S3, in the range of the scattering vector Q, from 0.001 to 0.1 Å^{-1} (length scale of 2.5–250 nm), and under dry conditions, the average slopes are −3.26 for the *Hymera* shale and −3.15 for the *Herrin* shale—corresponding to surface fractal dimensions f_D of 2.74 and 2.85, respectively. This indicates that the *Herrin* shale has rougher grain-grain and pore surfaces than the *Hymera* shale over the range in length scale 2.5–250 nm. The evolution of surface roughness at different relative humidities will be discussed subsequently in Sect. 3.2.2.

3.2 Impacts of Water Condensation in Anisotropic and Fractal Pores

Wetting fluid distribution within pores at a prescribed relative humidity (RH) can be described by two limiting regimes (Broseta et al. 2001; Steele et al. 1996), as schematically represented in Fig. 8. First, condensing fluid fills strongly curved concave surfaces (small radii) to form a capillary wetting regime (Broseta et al. 2001). This regime requires a significantly high pore irregularity (as quantified by fractal dimension) combined with adequate water content, surface tension, and wettability. The other limiting regime is to form a flat fluid film covering the entire pore surface and having a homogeneous thickness (Broseta et al. 2001). This limiting regime corresponds to a strong pore-fluid interaction, small pore irregularity and smooth surfaces. In this section, water condensation within anisotropic pore spaces is described based on the in situ SANS results with respect to the alignment factor, fractal dimension, and pore size distributions noted for the dry samples.

SANS scattering patterns for the two shales under different relative humidities are shown in Fig. 9 and Fig. 10. Compared to the dry condition, scattering intensity for the *Hymera* shale (Fig. 9) for $R_h \sim 41\%$ remains almost unchanged over the entire range of the scattering vector Q, except for a slight decrease at larger Q (>0.08 Å^{-1}). This suggests a slight condensation of water in pores with radii smaller than ~3 nm at a R_h of 41%. At a R_h of 83%, however, the intensity drops dramatically over the whole range of Q values, indicating the form of the water condensation over pore sizes in the range 1–250 nm. For the *Herrin* shale, as shown in Fig. 10, instead of a sharp decrease in intensity over the entire Q range at high relative humidity, negligible changes are observed in the scattering intensity for the *Herrin* shale over the smaller Q range, and there is a gradual decrease

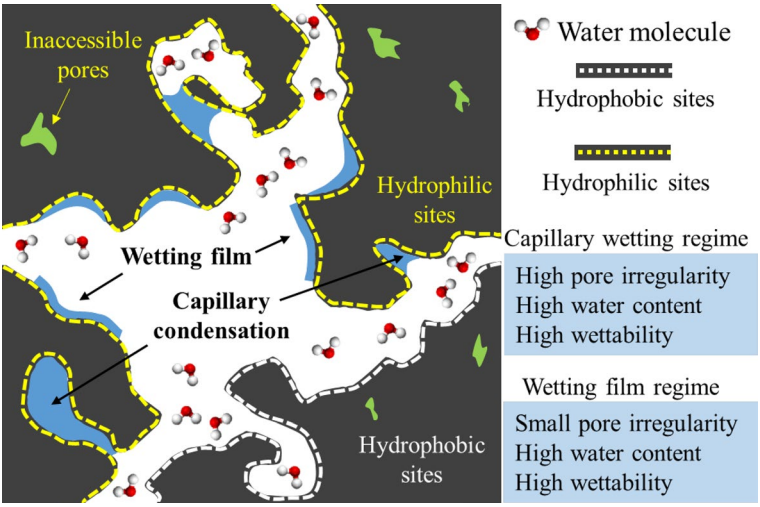

Fig. 8 Schematic of water condensation within heterogeneous pores in shale. The two limiting regimes, i.e., capillary wetting regime and wetting film regime, are determined by the pore irregularity, water content, and wettability (Broseta et al. 2001; Steele et al. 1996)

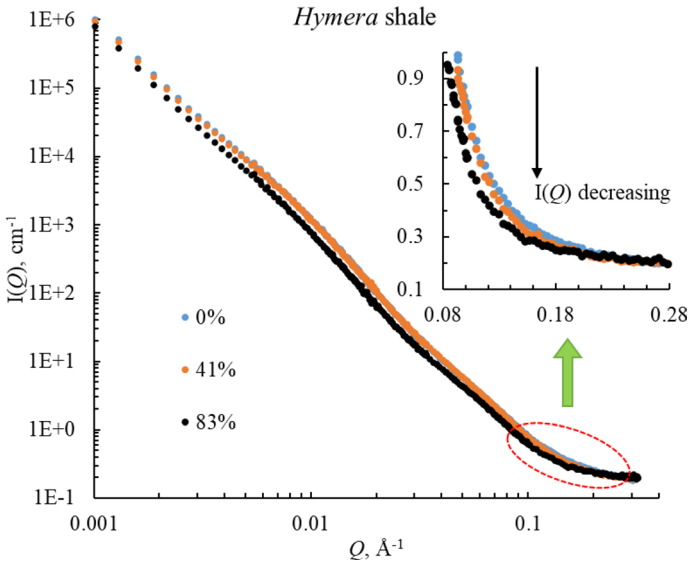

Fig. 9 SANS scattering profiles of the *Hymera* shale under relative humidities of 0%, 41%, and 83%, plotted as a function of the scattering vector Q. The insets are zoomed-in values for Q in the range 0.08–0.28 $Å^{-1}$

in intensity with increasing R_h in the higher Q range. This SANS scattering pattern, as a function of relative humidity, for the *Herrin* shale is consistent with that for Vosges sandstones (Broseta et al. 2001), revealing that water condenses in the most strongly curved asperities instead of covering the entire surface as a flat wetting film. Details of the water

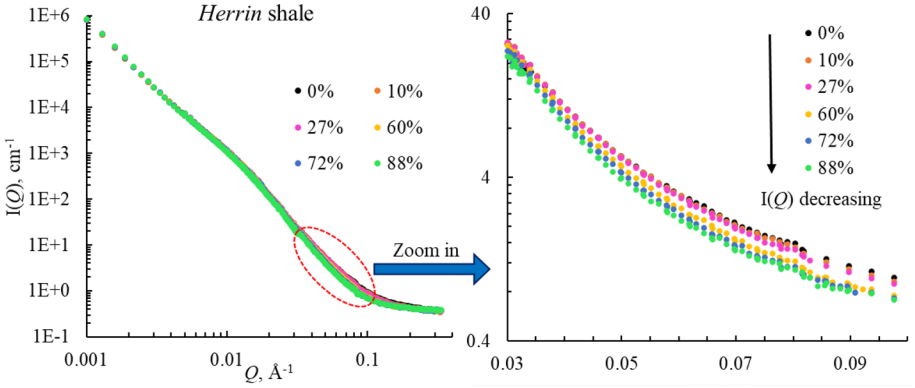

Fig. 10 SANS scattering profiles of the *Herrin* shale under different relative humidities, plotted as a function of the scattering vector Q with a zoomed-in view at Q in the range 0.03–0.1 Å^{-1}

sorption characteristics in shale pores are discussed in subsequent sections considering the evolution of the alignment factor, surface roughness, and pore size distribution. We also observe from Figs. 9 and 10 that the scattering curves exhibit a flat background at high Q (>0.2 Å^{-1}), possibly induced by incoherent scattering of hydrogen atoms in minerals/kerogens or micro-scale inhomogeneities (Bahadur et al. 2014; Mastalerz et al. 2012). The higher flat background at higher relative humidity indicates more incoherent scattering of hydrogen atoms due to adsorbed water on the mineral/particle surfaces or on water condensed in the micropores. In this study, the incoherent scattering background is subtracted (Clarkson et al. 2013; Stefanopoulos et al. 2017) for the interpretation of pore anisotropy, surface roughness, and pore size distribution.

3.2.1 Decrease in Pore Anisotropy

Figure 11 shows scattering intensity plotted with azimuthal angle under different R_h values for a scattering vector Q of 0.06 Å^{-1} (pore radii ~4.2 nm). For the *Hymera* shale, scatting intensity shows a slight change at R_h ~ 41%, with an obvious drop at R_h ~ 83%, likely due to water condensation. Scattering intensity of the *Herrin* shale decreases progressively

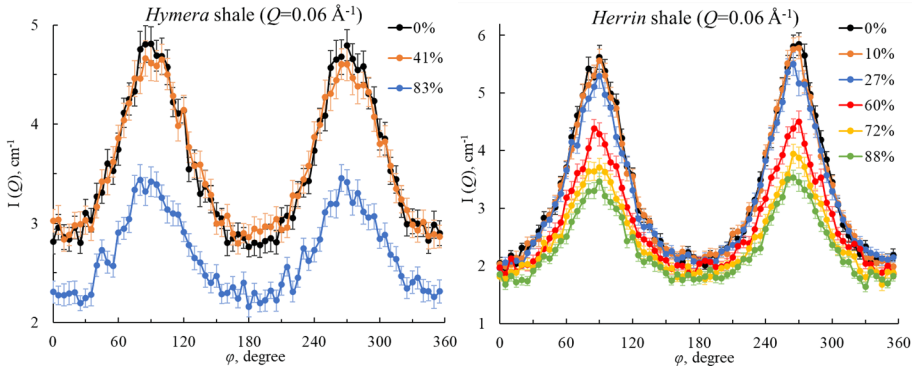

Fig. 11 Scattering intensity $I(\varphi)$ versus azimuthal angle φ for different relative humidities at $Q = 0.06$ Å^{-1}

with increasing R_h at this Q value. These trends are consistent with the SANS patterns at this Q range shown in Figs. 9 and 10. The variation in scattering intensities at different azimuthal angles indicates preferentially aligned pore structures. Equation (2) was used to determine the alignment factors for different mesopore radii (2.5 nm, 3.1 nm, 4.2 nm, 6.3 nm, 12.5 nm, 16.7 nm, 25 nm), corresponding to selected Q values of 0.01, 0.015, 0.02, 0.04, 0.06, 0.08, and 0.1 $Å^{-1}$, as a function of relative humidity (Fig. 12). Overall, the alignment factor decreases with increasing relative humidity for the two tested shales, suggesting that water condensation within pore spaces tends to "isotropize" the preferentially oriented pores. Considering that the SLD of the liquid D_2O/H_2O mixture is equal to that of the shale matrix and that pore orientation is free from the effect of water condensation, the decreasing alignment factors with increasing R_h values may be due either to the presence of a thicker wetting film on the walls or due to capillary condensation that completely fills the pore space. Both the two possible mechanisms reduce the aspect ratio of the non-equiaxed pores and decrease the resulting pore anisotropy as a result of water condensation. Understanding this "isotropizing" effect is important since it potentially influences porohydromechanical properties such as relative permeability and damage in anisotropic shales and other related media (Kwon et al. 2004; Shao et al. 2005).

Since the *Hymera* shale contains only hydrophilic minerals, the Kelvin radius for capillary condensation in the *Hymera* shale can be evaluated as 5.6 nm at an R_h of 83% and a temperature of 23 °C. Pores with radii of curvature larger than 5.6 nm tend to be covered by thin wetting films, while those with radii of curvature smaller than 5.6 nm will be filled with capillary water. Alignment factors in the *Herrin* shale for larger mesopores (pore radii of 12.5 nm, 16.7 nm, and 25 nm) remain almost unchanged at different humidity conditions (0–88%), indicating that water condensation in these pores has an insignificant effect. For smaller mesopores (pore radii of 6.3 nm, 4.2 nm, 3.1 nm, and 2.5 nm), the alignment factor shows a progressive decrease with increasing R_h and approaches a constant value for $R_h > 72$–88%. At lower relative humidity, wetting films cover the hydrophilic pore/particle surfaces. As humidity increases, the thickness of the wetting film grows until the pores are totally filled with condensed water, at which stage (>72%) the alignment factor approaches a constant value as relative humidity is further increased (88%). This is also consistent with the trend of change in the alignment factor at R_h of 72 and 88% that the smaller the pore radii, the closer the alignment factor is to a constant. At the highest relative humidity (83% for the *Hymera* shale and 88% for the *Herrin* shale), the alignment factors for the selected

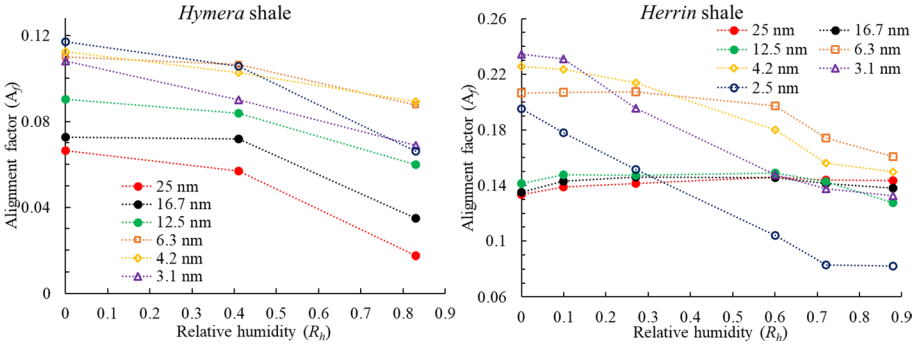

Fig. 12 Evolution of alignment factor as a function of relative humidity for the two shales at different pore scales (Q from 0.01 to 0.1 $Å^{-1}$)

length scales have still not reached zero—this may result from either the inaccessibility of pores and/or the presence of hydrophobic kerogen pores where no condensation occurs at high relative humidity, as shown in Fig. 8. The accessibility of shale pores, which is not addressed in this study, can be estimated by SANS studies based on liquid H_2O/D_2O mixtures or high-pressure CD_4 injection (Bahadur et al. 2014; Liu et al. 2019; Melnichenko et al. 2012; Ruppert et al. 2013). Regardless, the presence of both hydrophilic clays and hydrophobic kerogen in the *Herrin* shale renders discriminating between pores covered by wetting films or filled with condensation products a challenge, due to the wetting heterogeneity (Hiller et al. 2019; Van Lingen et al. 1996).

3.2.2 Surface Roughness Due to Water Condensation for Tested Shales

Fractal dimensions for these two shales under different humidities were estimated from the SANS scattering pattern over the Q range of 0.001–0.1 $Å^{-1}$ (length scale of 2.5–250 nm). As shown in Fig. 13, for R_h of 41% and 83%, the fractal dimension of the *Hymera* shale remains almost constant, indicating that condensing water covers the surface with a wetting film instead of totally filling strongly curved asperities (Broseta et al. 2001; Cheng et al. 1989). The surface roughness of the *Herrin* shale, as quantified by the fractal dimension f_D, decreases continuously with an increase in relative humidity. This "smoothing" effect is primarily induced by water condensing and filling-in strongly curved asperities (Broseta et al. 2001; Cheng et al. 1989). Different from previous studies where a Porod behavior of a smooth pore-matrix interfaces ($f_D=2$) is observed at smaller length scales (Broseta et al. 2001), the surface roughness of the *Herrin* shale does not disappear ($f_D>2$) even at an R_h of 88%. There are several possible explanations for this behavior. Firstly, shale heterogeneity due to various mineralogical compositions results in rough pore-particle interfaces where contrast matching can never be fully achieved. Secondly, variations of wettability among clays, kerogen, and other minerals induce a strong wetting heterogeneity of the shale and hence the water will only condense at strongly hydrophilic pore-mineral interfaces and not at hydrophobic pore-kerogen interfaces. In this case, water can only "defractalize" the strongly curved pores in hydrophilic clays while hydrophobic kerogen pores will retain rough surfaces, which are still detectable by SANS. Lastly, inaccessible pores may also contribute, to some extent, to the rough surfaces which are free from condensation—as they are inaccessible to the water. The effect of inaccessible pores may be eliminated by subtracting the scattering intensity measured under vacuum from the scattering intensity

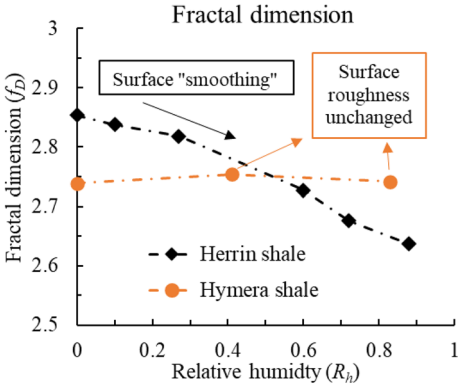

Fig. 13 Evolution of fractal dimension as a function of relative humidity for the two shales

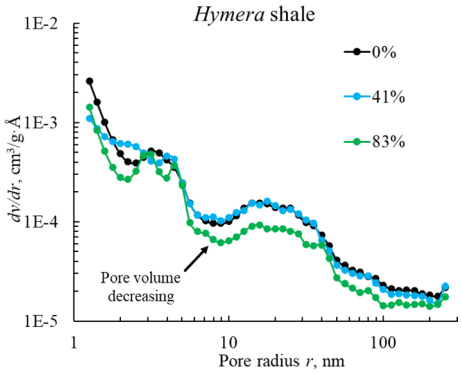

Fig. 14 Differential distributions of pore volume for the *Hymera* shale under relative humidities of 0%, 41%, and 83%, based on a polydisperse spherical (PDSP) model

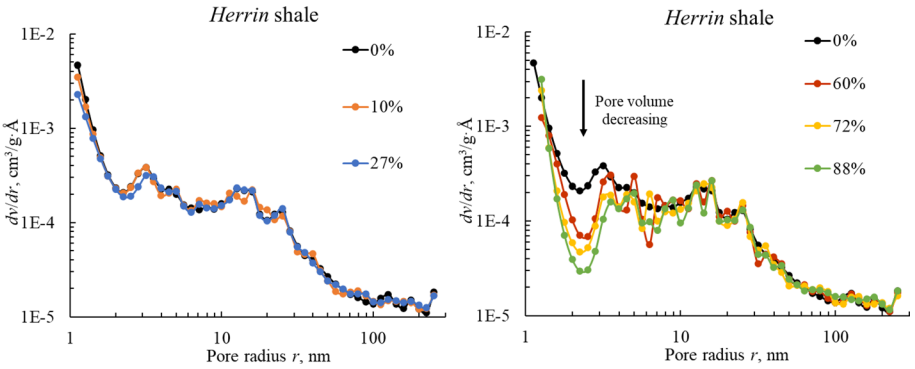

Fig. 15 Differential distributions of pore volume for the *Herrin* shale under relative humidities of 0%, 10%, 27%, 60%, 72%, and 88%, based on a polydisperse spherical (PDSP) model

under contrasting conditions. Unfortunately, the effect of inaccessible pores is ignored both in this study and previous studies (Broseta et al. 2001)—leaving this to future studies to quantify the role of inaccessible pores on water condensation behavior.

3.2.3 Pore Size Distribution

A polydisperse spherical particle (PDSP) model, as implemented in the PRINSAS software (Hinde 2004; Radlinski 2006), is used to retrieve the pore size distributions for the imaged media under different humidity conditions. For the *Hymera* shale, pore volume distribution is invariant at relative humidities of 0% and 41% (Fig. 14), indicating that water condensation is excluded below a relative humidity of 41%. For $R_h < 83\%$, however, a significant decrease in pore volume is observed over a large range of pore sizes (radii from 1 to 250 nm). Considering that the surface roughness of the *Hymera* shale for $R_h < 83\%$ remains near constant (Fig. 13), the decrease in pore volume over the wide pore size range is mainly due to the uniform coverage of a wetting film over the pore surfaces. For the *Herrin* shale, differential distributions of pore volume (Fig. 15) are essentially unchanged at relative humidity values of 10% and 27% except that smaller mesopore volumes (~1 nm in radius) slightly decrease with increasing humidity. Under increasing relative humidities of 60%,

72%, and 88%, mesopore volumes of radii in the range 1–10 nm significantly decrease the increase in relative humidity. This indicates that condensation occurs in mesopores of radii < 10 nm as relative humidity increases. From Fig. 15, there is negligible change in the volume of large pores (radii > 10 nm). The decrease in the pore size distribution, for radii in the range 1–250 nm for the *Hymera* shale and in the range 1–10 nm for the *Herrin* shale, indicates that water condensation "homogenizes" the shale pore architecture by narrowing the pore volume over these pore size ranges.

3.3 Water Condensation Behavior in Large Pores by USANS

USANS patterns under different humidity conditions determine the water condensation behavior in the large pore architecture. 1-D slit-smeared USANS data were measured under different humidity conditions in the direction perpendicular to the bedding planes (Supporting information Figure S4 and S5). Due to the mismatch in the humidity conditions relative to that for the SANS experiment, we discuss the USANS data (smaller Q ranges) separately, without merging them with the SANS data (detailed extensively in the earlier sections). USANS scattering intensity for the *Hymera* shale at a relative humidity of 33% remains almost identical as under the dry condition—water condensation is practically absent for large pores (radii ≥ 250 nm). At $R_h \sim 83\%$, a slight decrease of the scattering intensity occurs at $Q \geq 1.3\text{e}{-4}$ Å^{-1}, corresponding to water condensation on pore (≤1.9 μm) surfaces. In such large pores, it is difficult to form a capillary regime, due to the lack of small radius curvature (i.e. from Kelvin theory). Instead, the wetting film may form at the hydrophilic pore surfaces due to a strong pore-water interaction. Based on both Figure S4 (Supporting information) and Fig. 9, scattering intensity at $R_h \sim 83\%$ decreases over a broad range of scattering vectors from 1.3e–4 Å^{-1} to 0.2 Å^{-1} (pore radii 1.3 nm–1.9 μm). This is considerably different from the scattering intensity for the *Herrin* shale, which remains almost unchanged over Q ranges from 3e−5 to 0.001 Å^{-1} (pore radii 250 nm–8.3 μm) for USANS profiles for $R_h < 75\%$ (Supporting information Figure S5) and from 0.001 to 0.025 Å^{-1} (10–250 nm) for SANS profiles for $R_h < 88\%$ (Fig. 10). This indicates that water barely condenses in the larger pores for the *Herrin* shale, which is also consistent with the previous observation that water condensation in larger mesopores (radii 10–25 nm) and macropores (radii > 25 nm) is insignificant (Fig. 15).

3.4 Condensation Behavior Across the Scales: SANS vs. DVS

Dynamic water vapor sorption (DVS) isotherms were obtained at 23 °C by measurement of the mass change in shale powder samples under different relative humidities. The experimental procedures can be found in our previous study (Sang et al. 2019). The results, shown in Fig. 16, indicate that overall saturation estimated from SANS is lower than that recovered by DVS. There are two possible reasons for the underestimation of water vapor sorption estimated from the SANS data. First, micropore filling occurs in even the smallest of the small pores/rough-surfaces (radii < 1 nm), including those below the measurement resolution of USANS/SANS—this is an intrinsic limit in the scattering intensity at high Q where signal and incoherent background noise can no longer be separated. Second, cation hydration in clay minerals increases the surface area and hence provides more sites for water vapor adsorption. The presence of this invisible surface area, developed as a result of complex surface chemistry, has been demonstrated previously (Aylmore and Quirk 1967; Diamond and Kinter 1956; Sang et al. 2019). In particular, for the *Herrin* shale containing

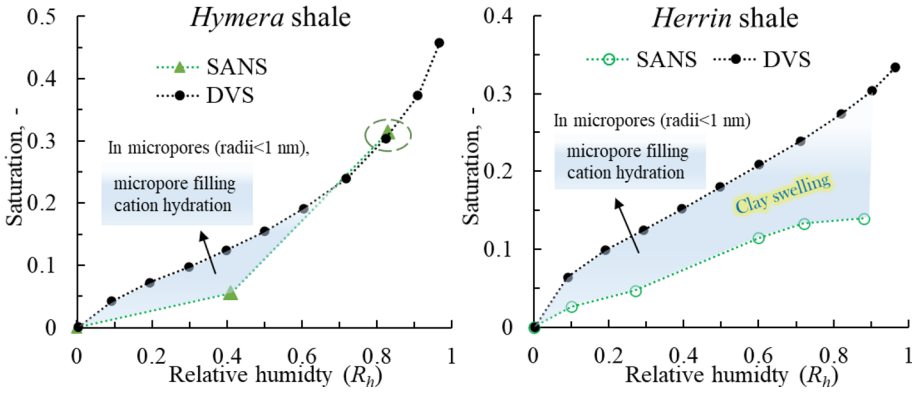

Fig. 16 Degree of saturation estimated by SANS and dynamic water vapor sorption (DVS) isotherms

8.6% montmorillonite, cation hydration in the interlamellar spaces and hydration-induced interlayer swelling at microscale (radii < 1 nm) could result in a dramatic contribution to total water adsorption potential, as illustrated in Figure S6 (Supporting information). Also, as suggested by the X-ray diffraction patterns of montmorillonite under controlled humidity (Cases et al. 1992), two or three sheets of water sheets may form in the interlamellar space (causing swelling) at R_h between 0.5 and 0.93. Clay swelling in the *Herrin* shale is likely the major factor controlling the dramatic underestimation of the saturation by SANS techniques. For the *Hymera* shale absent expansive clays, saturations evaluated from SANS data match those based on the DVS method at least at high relative humidity (83%), suggesting that the contribution of cation hydration and micropore filling to the total water adsorption is insignificant at high relative humidity. As shown in Fig. 14 and in Figure S4, water film covers almost an entire pore size classification (pore radii from ~ 1 nm to ~ 1.9 μm) for the *Hymera* shale at an R_h of 83%, contributing to the dominant role of water adsorption relative to micropore filling and cation hydration (Fig. 16). To summarize, USANS/SANS techniques work well to characterize water condensation behavior in shale mesopore/macropores. For samples containing high clay content and a large number of micropores, SANS techniques are incapable of precisely estimating the complete water sorption behavior.

4 Conclusion

In situ ultra-small/small-angle neutron scattering techniques were applied to study the water condensation behavior in shales exposed to a vapor of contrast-matching water. This is achieved by characterizing the evolution of pore orientation and anisotropy, fractal characteristics of pore surfaces, and pore size distribution of two contrasting organic-rich and inorganic shales, both dry and under a spectrum of relative humidities (up to 88%). Several main conclusions are drawn as follows.

Pores in shale are typically non-equiaxed (i.e. aspect ratio >1) and are anisotropically oriented, preferentially with long axes parallel to bedding, and support fractal interfaces. The *Hymera* shale's lack of organic matters exhibits a broadly decreasing anisotropy, corresponding to a decreasing preferential orientation of non-equiaxed pores, with an increase

of pore radii from 2.5 to 125 nm. The organic-rich *Herrin* shale also exhibits a decrease in anisotropy with an increase in pore size at the mesoscale (pore radii < 25 nm) but increasing anisotropy at macroscale (pore radii > 25 nm). Compared to the *Hymera* shale, the organic-rich *Herrin* shale exhibits a higher pore anisotropy and comprises rougher pore surfaces over length scales in the range 2.5–250 nm. SEM–EDS analysis also confirms that *Herrin* shale presents more anisotropic microfabrics and higher heterogeneity than *Hymera* shale.

The distribution of pore volumes decreases with increasing relative humidity, implicating water condensation in multi-scale shale pores. For the *Hymera* shale with less wetting heterogeneity, a wetting film uniformly covers the pore-matrix interface over a wide range of scale (~1 nm–1.9 μm) without smoothing/defractalizing the pore surfaces. For the *Herrin* shale with highly heterogeneous wetting characteristics, mesopore (radii of 1–10 nm) condensation occurs on strongly curved hydrophilic asperities and tends to smooth the surface roughness. Regardless of the form of either the flat wetting film on pore-matrix surfaces or the condensed water in-filling the pore volume, the impact of water condensation is to homogenize and isotropize the pore structures by narrowing the pore volume and reducing the aspect ratio of the non-equiaxed pores.

Finally, USANS/SANS techniques are capable of characterizing water condensation characteristics in shale mesopore/macropores based on contrast-matching water vapor sorption. However, the limitation is that they may underestimate the total water adsorption due to the involvement of micropore filling, cation hydration, and clay swelling processes, operating at the micropore scale (pore radii <1 nm).

Acknowledgements Access to ultra-small/small-angle neutron scattering instruments was provided by the Center for High Resolution Neutron Scattering, a partnership between the National Institute of Standards and Technology and the National Science Foundation under Agreement No. DMR-1508249. The authors also thank Bradley Frieberg and Yun Liu from NCNR for their generous help in the setup of the controlled-humidity cell and in related USANS/SANS measurements. These acknowledgments imply no recommendation nor endorsement by the National Institute of Standards and Technology, nor does it imply that the products identified are necessarily the best available for the purpose.

Author Contributions Shimin Liu and Derek Elsworth led the project. Guijie Sang, Rui Zhang, and Markus Bleuel conceived the method and performed USANS/SANS experiments. Guijie Sang and Shimin Liu performed the DVS experiment and the data analysis. All authors analyzed the USNAS/SANS results and contributed to the scientific discussions and manuscript writing.

Funding This work is financially supported by The National Institute of Occupational Safety and Health (NIOSH) under contract No. NIOSH-200-2016-90385.

Availability of Data and Material The data used in this paper can be downloaded from the Zenodo website (https://doi.org/10.5281/zenodo.4127235).

Code Availability Not applicable.

Compliance with Ethical Standards

Conflict of Interest The authors declare that they have no conflict of interest.

References

AlRatrout, A., Blunt, M.J., Bijeljic, B.: Wettability in complex porous materials, the mixed-wet state, and its relationship to surface roughness. Proc. Natl. Acad. Sci. **115**, 8901–8906 (2018)

Andrew, M., Bijeljic, B., Blunt, M.J.: Pore-by-pore capillary pressure measurements using X-ray microtomography at reservoir conditions: Curvature, snap-off, and remobilization of residual CO 2. Water Resour. Res. **50**, 8760–8774 (2014)
Anovitz, L.M., Cole, D.R., Sheets, J.M., Swift, A., Elston, H.W., Welch, S., Chipera, S.J., Littrell, K.C., Mildner, D.F.R., Wasbrough, M.J.: Effects of maturation on multiscale (nanometer to millimeter) porosity in the Eagle Ford Shale. Interpretation. **3**, SU59–SU70 (2015)
Aylmore, L.A.G., Quirk, J.P.: The micropore size distributions of clay mineral systems. J. Soil Sci. **18**, 1–17 (1967)
Bahadur, J., Melnichenko, Y.B., Mastalerz, M., Furmann, A., Clarkson, C.R.: Hierarchical pore morphology of cretaceous shale: a small-angle neutron scattering and ultrasmall-angle neutron scattering study. Energy Fuels **28**, 6336–6344 (2014)
Bale, H.D., Schmidt, P.W.: Small-angle X-ray-scattering investigation of submicroscopic porosity with fractal properties. Phys. Rev. Lett. **53**, 596 (1984)
Barrett, E.P., Joyner, L.G., Halenda, P.P.: The determination of pore volume and area distributions in porous substances. I. Computations from nitrogen isotherms. J. Am. Chem. Soc. **73**, 373–380 (1951)
Blunt, M., King, P.: Relative permeabilities from two-and three-dimensional pore-scale network modelling. Transp. porous media. **6**, 407–433 (1991)
Bousige, C., Ghimbeu, C.M., Vix-Guterl, C., Pomerantz, A.E., Suleimenova, A., Vaughan, G., Garbarino, G., Feygenson, M., Wildgruber, C., Ulm, F.-J.: Realistic molecular model of kerogen's nanostructure. Nat. Mater. **15**, 576–582 (2016)
Broseta, D., Barré, L., Vizika, O., Shahidzadeh, N., Guilbaud, J.-P., Lyonnard, S.: Capillary condensation in a fractal porous medium. Phys. Rev. Lett. **86**, 5313 (2001)
Byers, C.W.: Shale fissility: relation to bioturbation. Sedimentology **21**, 479–484 (1974). https://doi.org/10.1111/j.1365-3091.1974.tb02073.x
Byers, C.W.: Geological significance of marine biogenic sedimentary structures. Anim. Sedim. Relat. **100**, 221–256 (1982). https://doi.org/10.1007/978-1-4757-1317-6_5
Cases, J.M., Bérend, I., Besson, G., Francois, M., Uriot, J.P., Thomas, F., Poirier, J.E.: Mechanism of adsorption and desorption of water vapor by homoionic montmorillonite. 1. The sodium-exchanged form. Langmuir **8**, 2730–2739 (1992)
Cheng, E., Cole, M.W., Pfeifer, P.: Defractalization of films adsorbed on fractal surfaces. Phys. Rev. B. **39**, 12962 (1989)
Chiang, W.-S., Georgi, D., Yildirim, T., Chen, J.-H., Liu, Y.: A non-invasive method to directly quantify surface heterogeneity of porous materials. Nat. Commun. **9**, 1–7 (2018)
Chichinina, T.I., Obolentseva, I.R., Ronquillo-Jarillo, G.: Anisotropy of seismic attenuation in fractured media: theory and ultrasonic experiment. Transp. Porous Media. **79**, 1–14 (2009)
Clarkson, C.R., Solano, N., Bustin, R.M., Bustin, A.M.M., Chalmers, G.R.L., He, L., Melnichenko, Y.B., Radliński, A.P., Blach, T.P.: Pore structure characterization of North American shale gas reservoirs using USANS/SANS, gas adsorption, and mercury intrusion. Fuel **103**, 606–616 (2013)
Diamond, S., Kinter, E.B.: Surface areas of clay minerals as derived from measurements of glycerol retention. Clays Clay Miner. **5**, 334–347 (1956)
Elsworth, D., Spiers, C.J., Niemeijer, A.R.: Understanding induced seismicity. Science **354**, 1380–1381 (2016)
Eveline, V.F., Akkutlu, I.Y., Moridis, G.J.: Numerical simulation of hydraulic fracturing water effects on shale gas permeability alteration. Transp. Porous Media. **116**, 727–752 (2017)
Fisher, L.R., Gamble, R.A., Middlehurst, J.: The Kelvin equation and the capillary condensation of water. Nature **290**, 575 (1981)
Ghassemi, A., Diek, A.: Porothermoelasticity for swelling shales. J. Pet. Sci. Eng. **34**, 123–135 (2002)
Gu, X., Cole, D.R., Rother, G., Mildner, D.F.R., Brantley, S.L.: Pores in Marcellus shale: a neutron scattering and FIB–SEM study. Energy Fuels **29**, 1295–1308 (2015)
Hall, P.J., Antxustegi, M., Ruiz, W.: Contrast-matching small-angle neutron scattering evidence for the absence of a connected pore system in Pittsburgh No. 8 coal. Fuel **77**, 1663–1665 (1998)
Hall, P.L., Mildner, D.F.R., Borst, R.L.: Small-angle scattering studies of the pore spaces of shaly rocks. J. Geophys. Res. Solid Earth. **91**, 2183–2192 (1986)
Hannon, M.J., Finsterle, S.: The effect of anisotropy on multi-dimensional pressure-pulse-decay experiments. Transp. Porous Media. **123**, 545–562 (2018)
Hesselbo, S.P., Gröcke, D.R., Jenkyns, H.C., Bjerrum, C.J., Farrimond, P., Bell, H.S.M., Green, O.R.: Massive dissociation of gas hydrate during a Jurassic oceanic anoxic event. Nature **406**, 392 (2000)
Hiller, T., Ardevol-Murison, J., Muggeridge, A., Schröter, M., Brinkmann, M.: The impact of wetting-heterogeneity distribution on capillary pressure and macroscopic measures of wettability. SPE J. **24**, 200–214 (2019)

Hinde, A.L.: PRINSAS: a Windows-based computer program for the processing and interpretation of small-angle scattering data tailored to the analysis of sedimentary rocks. J. Appl. Crystallogr. **37**, 1020–1024 (2004)

Hongladarom, K., Ugaz, V.M., Cinader, D.K., Burghardt, W.R., Quintana, J.P., Hsiao, B.S., Dadmun, M.D., Hamilton, W.A., Butler, P.D.: Birefringence, X-ray scattering, and neutron scattering measurements of molecular orientation in sheared liquid crystal polymer solutions. Macromolecules **29**, 5346–5355 (1996)

Kuila, U., Prasad, M.: Specific surface area and pore-size distribution in clays and shales. Geophys. Prospect. **61**, 341–362 (2013)

Kwon, O., Kronenberg, A.K., Gangi, A.F., Johnson, B., Herbert, B.E.: Permeability of illite-bearing shale: 1. Anisotropy and effects of clay content and loading. J. Geophys. Res. Solid Earth **109**, 1–19 (2004)

Lahn, L., Bertier, P., Seemann, T., Stanjek, H.: Distribution of sorbed water in the pore network of mudstones assessed from physisorption measurements. Microporous Mesoporous Mater. **295**, 109902 (2020)

Lash, G.G., Blood, D.R.: Origin of shale fabric by mechanical compaction of flocculated clay: evidence from the Upper Devonian Rhinestreet Shale, western New York, USA. J. Sediment. Res. **74**, 110–116 (2004)

Leu, L., Georgiadis, A., Blunt, M.J., Busch, A., Bertier, P., Schweinar, K., Liebi, M., Menzel, A., Ott, H.: Multiscale description of shale pore systems by scanning SAXS and WAXS microscopy. Energy Fuels **30**, 10282–10297 (2016)

Liu, S., Zhang, R.: Anisotropic pore structure of shale and gas injection-induced nanopore alteration: a small-angle neutron scattering study. Int. J. Coal Geol. **219**, 103384 (2020)

Liu, S., Zhang, R., Karpyn, Z., Yoon, H., Dewers, T.: Investigation of accessible pore structure evolution under pressurization and adsorption for coal and shale using small-angle neutron scattering. Energy Fuels **33**, 837–847 (2019)

Loon, V.L.R.: Preferred orientations and anisotropy in shales: Callovo-Oxfordian shale (France) and Opalinus Clay (Switzerland). Clays Clay Miner. **56**, 285–306 (2008)

Luzar, A., Chandler, D.: Hydrogen-bond kinetics in liquid water. Nature **379**, 55 (1996)

Mastalerz, M., He, L., Melnichenko, Y.B., Rupp, J.A.: Porosity of coal and shale: Insights from gas adsorption and SANS/USANS techniques. Energy Fuels **26**, 5109–5120 (2012)

Melnichenko, Y.B., He, L., Sakurovs, R., Kholodenko, A.L., Blach, T., Mastalerz, M., Radliński, A.P., Cheng, G., Mildner, D.F.R.: Accessibility of pores in coal to methane and carbon dioxide. Fuel **91**, 200–208 (2012)

O'Brien, N.R.: The effects of bioturbation on the fabric of shale. J. Sediment. Petrol. **57**, 449–455 (1987). https://doi.org/10.1306/212f8b5c-2b24-11d7-8648000102c1865d

Radlinski, A.P.: Small-angle neutron scattering and the microstructure of rocks. Rev. Mineral. Geochemistry. **63**, 363–397 (2006)

Radliński, A.P., Boreham, C.J., Lindner, P., Randl, O., Wignall, G.D., Hinde, A., Hope, J.M.: Small angle neutron scattering signature of oil generation in artificially and naturally matured hydrocarbon source rocks. Org. Geochem. **31**, 1–14 (2000)

Radlinski, A.P., Boreham, C.J., Wignall, G.D., Lin, J.-S.: Microstructural evolution of source rocks during hydrocarbon generation: a small-angle-scattering study. Phys. Rev. B. **53**, 14152 (1996)

Radlinski, A.P., Mastalerz, M., Hinde, A.L., Hainbuchner, M., Rauch, H., Baron, M., Lin, J.S., Fan, L., Thiyagarajan, P.: Application of SAXS and SANS in evaluation of porosity, pore size distribution and surface area of coal. Int. J. Coal Geol. **59**, 245–271 (2004)

Radliński, A.P., Radlińska, E.Z., Agamalian, M., Wignall, G.D., Lindner, P., Randl, O.G.: Fractal geometry of rocks. Phys. Rev. Lett. **82**, 3078 (1999)

Ruppert, L.F., Sakurovs, R., Blach, T.P., He, L., Melnichenko, Y.B., Mildner, D.F.R., Alcantar-Lopez, L.: A USANS/SANS study of the accessibility of pores in the Barnett Shale to methane and water. Energy Fuels **27**, 772–779 (2013)

Sang, G., Liu, S., Elsworth, D.: Water vapor sorption properties of Illinois shales under dynamic water vapor conditions: experimentation and modeling. Water Resour. Res. **55**, 7212–7228 (2019). https://doi.org/10.1029/2019WR024992

Sang, G., Liu, S., Elsworth, D., Yang, Y., Fan, L.: Evaluation and modeling of water vapor sorption and transport in nanoporous shale. Int. J. Coal Geol. **228**, 103553 (2020). https://doi.org/10.1016/j.coal.2020.103553

Sang, G., Liu, S., Zhang, R., Elsworth, D., He, L.: Nanopore characterization of mine roof shales by SANS, nitrogen adsorption, and mercury intrusion: Impact on water adsorption/retention behavior. Int. J. Coal Geol. **200**, 173–185 (2018). https://doi.org/10.1016/j.coal.2018.11.009

Seemann, T., Bertier, P., Krooss, B.M., Stanjek, H.: Water vapour sorption on mudrocks. Geol. Soc. London, Spec. Publ. **454**, 201–233 (2017) (Spec. Publ.)
Shao, J.-F., Ata, N., Ozanam, O.: Study of desaturation and resaturation in brittle rock with anisotropic damage. Eng. Geol. **81**, 341–352 (2005)
Sposito, G., Skipper, N.T., Sutton, R., Park, S., Soper, A.K., Greathouse, J.A.: Surface geochemistry of the clay minerals. Proc. Natl. Acad. Sci. **96**, 3358–3364 (1999)
Steele, W.A., Zgrablich, G., Rudzinski, W.: Equilibria and dynamics of gas adsorption on heterogeneous solid surfaces. Elsevier, Amsterdam (1996)
Stefanopoulos, K.L., Youngs, T.G.A., Sakurovs, R., Ruppert, L.F., Bahadur, J., Melnichenko, Y.B.: Neutron scattering measurements of carbon dioxide adsorption in pores within the Marcellus shale: implications for sequestration. Environ. Sci. Technol. **51**, 6515–6521 (2017)
Van Eeckhout, E.M.: The mechanisms of strength reduction due to moisture in coal mine shales. Int. J. Rock Mech. Mining Sci. Geomech. **13**, 61–67 (1976)
Van Lingen, P.P., Bruining, J., Van Kruijsdijk, C.: Capillary entrapment caused by small-scale wettability heterogeneities. SPE Reserv. Eng. **11**, 93–100 (1996)
Van Loon, L.R., Soler, J.M., Müller, W., Bradbury, M.H.: Anisotropic diffusion in layered argillaceous rocks: a case study with Opalinus Clay. Environ. Sci. Technol. **38**, 5721–5728 (2004)
Wong, P., Howard, J., Lin, J.-S.: Surface roughening and the fractal nature of rocks. Phys. Rev. Lett. **57**, 637 (1986)
Yang, J., Hatcherian, J., Hackley, P.C., Pomerantz, A.E.: Nanoscale geochemical and geomechanical characterization of organic matter in shale. Nat. Commun. **8**, 1–9 (2017)
Zhang, R., Liu, S., Bahadur, J., Elsworth, D., Melnichenko, Y., He, L., Wang, Y.: Estimation and modeling of coal pore accessibility using small angle neutron scattering. Fuel **161**, 323–332 (2015)
Zhang, R., Liu, S., Wang, Y.: Fractal evolution under in situ pressure and sorption conditions for coal and shale. Sci. Rep. **7**, 8971 (2017)
Zhao, Y., Peng, L., Liu, S., Cao, B., Sun, Y., Hou, B.: Pore structure characterization of shales using synchrotron SAXS and NMR cryoporometry. Mar. Pet. Geol. **102**, 116–125 (2019)
Zolfaghari, A., Dehghanpour, H., Holyk, J.: Water sorption behaviour of gas shales: I. Role of clays. Int. J. Coal Geol. **179**, 130–138 (2017)
Zou, J., Rezaee, R., Yuan, Y., Liu, K., Xie, Q., You, L.: Distribution of adsorbed water in shale: an experimental study on isolated kerogen and bulk shale samples. J. Pet. Sci. Eng. **187**, 106858 (2020)

Affiliations

Guijie Sang[1] · Shimin Liu[1] · Derek Elsworth[1] · Rui Zhang[1] · Markus Bleuel[2,3]

[1] Department of Energy and Mineral Engineering, G3 Center and Energy Institute, The Pennsylvania State University, University Park, PA 16802, USA

[2] NIST Center for Neutron Research, National Institute of Standards and Technology, Gaithersburg, MD 20899, USA

[3] Department of Materials Science and Engineering, A. James Clark School of Engineering, University of Maryland, College Park, MD 20742, USA